Energy-Prediction-Based Co-Design and Control of Battery–Fuel-Cell Hybrid Powertrains for Long-Range Electric Coach Buses

CHOTALIYA, Keval, TASHAKOR, Nima <http://orcid.org/0000-0001-8052-9593>, POURHADI, Pouyan <http://orcid.org/0009-0002-8500-7633>, MUELLER, Uwe, ISSA, Walid <http://orcid.org/0000-0001-9450-5197> and GOETZ, Stefan <http://orcid.org/0000-0002-1944-0714>

International Journal of Energy Research

WILEY

RESEARCH ARTICLE OPEN ACCESS

Energy-Prediction-Based Co-Design and Control of Battery–Fuel-Cell Hybrid Powertrains for Long-Range Electric Coach Buses

Keval Chotaliya[1,2] | Nima Tashakor[3] | Pouyan Pourhadi[2] | Uwe Mueller[1] | Walid Issa[4] | Stefan Goetz[2]

[1]Freudenberg FST GmbH, Weinheim, Germany | [2]Department of Electrical and Computer Engineering, Rheinland-Pfälzische Technische Universität, Kaiserslautern, Germany | [3]Department of Electrical and Computer Engineering, Duke University, Durham, North Carolina, USA | [4]School of Engineering & Built Environment, Sheffield Hallam University, Sheffield, S1 1WB, UK

Correspondence: Nima Tashakor (nima.tashakor@duke.edu) | Pouyan Pourhadi (pourhadi@eit.uni-kl.de) | Stefan Goetz (goetz@eit.uni-kl.de)

Received: 7 February 2025 | **Revised:** 17 October 2025 | **Accepted:** 5 December 2025

Academic Editor: Denis Osinkin

Keywords: battery optimization | bounded-load-following control strategy (BLFCS) | energy management strategy (EMS) | energy-prediction-based control strategy (EPCS) | fuel-cell hybrid vehicle (FCHV)

ABSTRACT

Concerns over greenhouse gas emissions accelerate the shift to electric buses; yet battery-electric models often lack the range for long-haul transport. This paper studies a plug-in fuel-cell (FC) hybrid coach bus for a daily 650 km trip. The model integrates detailed FC, battery, and drive-unit dynamics with battery state-of-health (SoH) through capacity fade and resistance growth. Results demonstrate that the plug-in hybrid reduces consumption by 16.7% compared with a FC-only bus, whereas the 200 kWh battery provides a 100 kWh usable energy swing under an 85%–35% state of charge (SoC) period. Limiting the C-rate to 3C sets the minimum size at 190 kWh and confirms that energy, rather than power, determines the battery rating. A total-cost-of-ownership analysis over 12 years indicates that a € 100/kWh reduction in Li-ion price lowers cost by € 20,000 for the hybrid and by € 100,000 for a battery-electric bus. Well-to-wheel (WTW) emissions show that plug-in operation cuts greenhouse gases relative to both diesel and FC-only cases. These results establish a transparent framework for sizing and evaluating hybrid coaches across performance, cost, and emissions.

1 | Introduction

The transportation sector plays a pivotal role in global energy consumption and greenhouse gas emissions. In 2019, heavy-duty vehicles made up a small portion of vehicles on the road but were responsible for a large share of the 24% of CO_2 emissions from fuel combustion [1]. Buses, trucks, and other heavy-duty vehicles are essential for long-distance transport, but their diesel engines worsen environmental issues. This shift toward transportation electrification supports global efforts to tackle climate change [2].

Battery electric vehicles (BEVs) are effective at reducing emissions for light-duty vehicles but face challenges in heavy-duty, long-distance transport. Current batteries lack energy density for long-haul buses. Their large size, weight, and long charging times further reduce range and operational efficiency in long-distance transport. Although heavy-duty vehicle electrification has progressed, a typical BEV bus can travel only 400 km on a single charge, far short of the 600 km required for long-distance coach operations [3, 4].

Keval Chotaliya, Nima Tashakor, and Pouyan Pourhadi contributed equally to the paper.

Hydrogen-powered fuel-cell electric vehicles (FCEVs) offer a viable alternative in this context. FCs have higher energy densities than batteries and provide longer ranges. The higher energy density suggests them for heavy-duty applications. Nonetheless, FCs have substantial limitations, such as sensitivity to rapid power demand changes and the high cost of hydrogen infrastructure [5]. Combining FCs with battery systems may provide a practical solution to these challenges. The high energy density of hydrogen extends range, while batteries smoothen power fluctuations [6]. Designing an optimal FC hybrid system for long-range vehicles involves several challenges [7]. The first is determining the size of the energy storage components. An oversized battery increases vehicle weight and cost, whereas an undersized battery puts more load on the FC, which causes inefficiencies and a shorter lifespan. The second challenge is to develop an effective energy management strategy (EMS) to optimize hybrid system performance under different driving conditions.

Most research on hybrid energy systems examines urban buses and light-duty vehicles, with little focus on long-range applications such as coach buses. Studies on FC hybrids typically focus on control strategies for smaller vehicles and charge-sustaining operations. Moreover, most current energy management strategies, such as bounded-load-following control, keep the battery's state of charge (SoC) above a minimum threshold. However, this approach can make FC operation inefficient during long trips [8–16]. Odeim et al. [8] explored the use of multiobjective real-time genetic algorithms for hybrid power management, which improved system durability in transit buses by optimizing load distribution. Similarly, Hu et al. [9, 10] used convex programming to optimize power management in FCHVs. Their work focused on city buses, which have different energy and operational needs from long-range coach buses. Several studies [11–15] introduced energy management systems for hybrid buses that aim to minimize hydrogen consumption and reduce load fluctuations. Additionally, Wang et al. [16] presented a power management strategy which concurrently considers fuel consumption and the degradation of both the FC and battery. However, none of these strategies focus on long-distance applications, which have more complex and unpredictable energy demands and load patterns.

This gap shows the need for a solution to manage the energy challenges of long-range coach buses. A hybrid energy system for these applications must optimize efficiency, cost, and long-term reliability. It should balance the load between the battery and FC to extend their lifespan and maintain consistent performance on long journeys. We focus on two key innovations: (1) optimization of the battery and FC size to achieve a 650 km driving range and (2) development of an energy-prediction-based control strategy (EPCS) to reduce fuel consumption, extend component lifetimes, and improve system efficiency.

The hybrid system proposed in this study integrates a 200 kWh battery with a 150 kWh FC system. To ensure the system meets the demanding energy requirements of long-distance travel, we propose a novel control strategy that uses real-time energy predictions based on the driving route. The EPCS optimizes power distribution between the battery and FC. It allows the battery to handle peak loads and reduces the FC exposure to rapid load changes. This results in significant fuel savings and better operational efficiency compared to conventional bounded-load-following strategies. The contributions of this paper are as follows:

1. Optimization of the battery size (200 kWh) and FC system (150 kW) to meet long-haul transportation needs, which considers range, cost, and weight.
2. Proposal of an EPCS that optimizes power distribution, reduces fuel consumption by 16.7%, and extends the lifespan of both the FC and battery.

Section 2 presents the system and its modeling. Simulation in Section 3 verifies the analysis and evaluate the performance of the proposed system. Sections 4 and 5 provide the hybrid system sizing and EMS. Section 6 presents further results. Finally, Section 7 concludes the article.

2 | System Overview and Modeling

2.1 | System Introduction

This work considers the MCI D45 CRTe LE electric coach bus system manufactured by Motor Coach Industries [17]. Figure 1

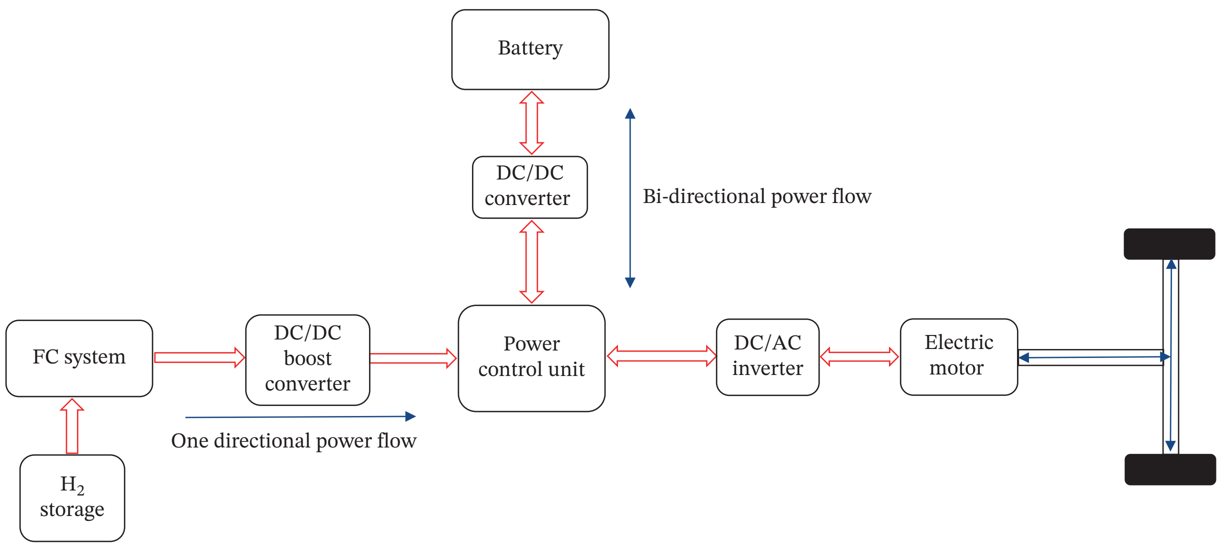

FIGURE 1 | Plug-in hybrid system topology.

shows the general overview of the modeled subsystems, which includes the FC, the battery, and the electric drive subsystems. Additionally, the electric drive subsystem comprises the electric motor, the required DC–DC converter, and inverter.

A single electric motor propels the hybrid bus, specifically the proton-exchange membrane (PEM) 1DB20924 manufactured by Siemens [17]. The electric motor drive gets a constant power supply from a low-temperature PEM FC. A large traction battery from XALT (XMP 76P high power pack) fulfills the peak power demand [18]. This work does not consider the power required for heat ventilation and air conditioning systems.

2.1.1 | Vehicle Type

The coach bus is a plug-in FC hybrid-electric vehicle (FCHV). To ensure efficient operation of the plug-in FCHV, it is recommended to charge the battery to a maximum defined as 85% SoC from grid electricity at the start of the journey and deplete it to the minimum defined as 35% SoC at the end of the trip.

2.1.2 | Hybrid System Topology

The battery and FC system can independently supply power to the electric motor. Two separate DC–DC converters are positioned after the FC and the battery to allow for a controllable DC bus. The nominal DC bus voltage is set to 750 V to match the motor's rated voltage [19]. A bidirectional DC–DC buck–boost converter is used between battery and electric motor. This bidirectional operation enables two functions: (i) supplying traction power when motor demand exceeds the constant FC output, and (ii) absorbing energy during regenerative braking, where negative motor power is fed back to the battery. The power flow of the FC system is unidirectional. Accordingly, a simpler unidirectional boost converter adjusts the voltage between the FC and the electric motor. The FC stack itself operates in the 350–500 V range, which is boosted by the unidirectional DC–DC converter to the 750 V DC bus. The boost conversion ensures compatibility with the motor's rated DC voltage and a low ripple on the FC. The battery pack is interfaced via a bidirectional buck–boost converter to the same 750 V bus. The power control unit can regulate and balance the instantaneous power drawn from the battery and FC system based on the power requirements of the electric motor and the energy control strategy. To streamline the modeling efforts, the inverter and the AC electric motor are designed as a single unit.

Figure 2 illustrates the configuration of the electric drive unit, which follows the same topology as the hybrid system. The electrical connection enables power flow from the FC system to both the motor and the battery, which depends on the control strategy. The buck–boost converter regulates the DC bus voltage, which is supplied to the electric motor. The battery serves as an electrical buffer in the electric drive system. Depending on the control logic of the surrounding components, the battery either supplies or receives power and accepts what the buck–boost controller delivers or draws. The system-level controller determines the power to be drawn from the FC system and supplies it to the DC bus. Table 1 summarizes the main electric motor parameters.

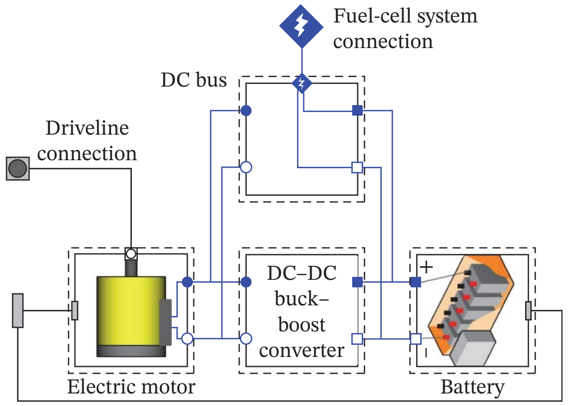

FIGURE 2 | Electric drive unit [20].

TABLE 1 | Electric motor parameters [8, 9].

Parameters	Notation	Value
Rated torque	T_{rated}	2700 Nm
Rated power	p_{rated}	260 kW
Maximum speed	$w_{\max}$	366 rad/s
Nominal DC voltage	$v_{\text{dc,nom}}$	750 V
Maximum DC	$i_{\text{dc,max}}$	600 A

2.2 | Modeling Tool

The model was developed using Modelon Impact, a software tool based on the Modelica system modeling language. The software provides various libraries used for this study. We mainly use the electrification, FC, vehicle dynamics, and the basic Modelica library. Table 2 lists the main properties of the vehicle model.

2.2.1 | Vehicle Longitudinal Dynamics

The traction force demand is calculated as follows:

$$F_{\text{t}} = m \cdot a + m \cdot \mu_{\text{roll}} \cos\theta + m \cdot g \sin\theta + \frac{1}{2}\rho A_{\text{f}} C_{\text{d}} v^2, \quad (1)$$

where m is the vehicle mass, a is acceleration, g is gravity, μ_{roll} is the rolling resistance coefficient, θ is road grade, ρ is the air density, A_{f} is the frontal area, C_d is the aerodynamic drag coefficient, and v is the speed [22].

TABLE 2 | Vehicle parameters [17, 21].

Parameters	Notation	Value
Gross vehicle weight of the coach bus	$\text{body}_{\text{mass}}$	24,000 kg
Aerodynamic drag coefficient (front)	$c_{w,\text{front}}$	0.6
Total length of the bus	Length	13.8 m
Front cross-sectional area of the bus	a_{front}	9 m^2
Rolling resistance friction coefficient	μ_{roll}	0.01

The required mechanical wheel power is then given as:

$$P_{\text{wheel}} = F_{\text{t}}.v, \tag{2}$$

which is supplied by the electric motor through the driveline efficiencies. This wheel demand links the vehicle dynamics to the energy supplied by the battery and FC system.

2.2.2 | Electric Drive Unit: (A) Motor and Inverter

The mechanical demand at the shaft is (Table 1):

$$P_{\text{mech}} = T \cdot w, T \leq T_{\text{rated}} \text{ and } w \leq w_{\max}, \tag{3}$$

where T and w are the torque and angular speed. The DC-side electrical power is then,

$$P_{\text{dc,mot}} = \frac{P_{\text{mech}}}{\eta_{\text{mot}} \cdot \eta_{\text{inv}}}, \tag{4}$$

with motor and inverter efficiencies assumed constant at $\eta_{\text{mot}} = 0.95, \eta_{\text{inv}} = 0.92,$ consistent with manufacturer data and typical EV modeling practice. These factors are also applied in the battery sizing relations in Section 4.

2.2.3 | Electric Drive Unit: (B) Converters

Figure 3 shows the DC–DC boost converter controller, which regulates the current drawn from the FC system. The controller takes four inputs: motor current, motor voltage, FC stack voltage, and battery SoC. Since the FC can only provide positive power, the motor current is filtered to include only positive values, and the max block ensures that negative motor power is treated as zero. So, the limit for FC current demand is set to zero and no negative values can be requested from the FC. Considering that the motor voltage and the FC stack voltage may differ, the magnitudes of the current values of the motor and the FC also differ. To solve the discrepancy, the factor k_{m}, which is the ratio of the motor voltage and the FC stack voltage, adjustes the motor current. We use average models with constant efficiency. The current drawn from the FC is regulated according to:

$$V_{\text{FC}} I_{\text{FC}} \eta_{\text{boost}} = V_{\text{Motor}} I_{\text{Motor}}, k_m = \frac{V_{\text{Motor}}}{V_{\text{FC}}}, \tag{5}$$

with efficiency $\eta_{\text{boost}} = 0.92$. The FC current is further limited by $i_{\text{FC}} \leq i_{\max}$, and a 5-s start-up delay is applied.

The source model incorporates the energy management algorithm, which determines the FC current to be drawn based on the control strategy. However, as the FC system cannot provide an intermittent current, a filter component is introduced to decrease the derivative of the current signal or smooth out the signal before it is supplied to the signal bus. Additionally, the index component is used to define which side of the DC–DC boost converter controller needs to be controlled. The FC demand current and the index values are transmitted to the FC-side DC–DC boost converter. The index value is set to 1, which regulates the incoming current from the FC stack to the converter.

The battery-side relation is:

$$p_{\text{BT}} = v_{\text{BT}} i_{\text{BT}}, v_{\text{bus}} = \frac{D}{1 - D} v_{\text{BT}}, \tag{6}$$

with efficiency $\eta_{\text{buck-boost}} = 0.92$. We adopted the sign convention $P_{\text{BT}} \leq 0$ during regeneration. This is consistent with the global hybrid power balance as follows:

$$P_{\text{BT}} = P_{\text{dc,mot}} - P_{\text{FC}}, \tag{7}$$

which links the motor, battery, and FC power flows.

2.2.4 | Electric Drive Unit: (C) Battery Model

The battery uses 1296 XALT XMP-76P cells in a 216s 6p configuration (200 kWh; Tables 3 and 4). A single equivalent cell is scaled to represent the pack behavior. The cell open-circuit voltage (OCV) follows the extended Shepherd relation:

$$v_{\text{out}} = v_{\text{cell,max}} - \frac{k}{\text{SoC}} + A e^{-B(1-\text{SoC})}, \tag{8}$$

where $v_{\text{cell,max}} = 4.2\,v$ is the maximum cell voltage, k is the polarization constant, and SoC is the state of charge [20]. The coefficients A and B capture exponential voltage behavior and SoC dynamics per,

$$A = v_{\text{cell,max}} - v_{\text{cell,exp}}, \; B = \frac{3}{\frac{q_{\text{cell, exp}}}{q_{\text{cell,max}}}}, \tag{9}$$

where $v_{\text{cell,exp}}$ is the exponential voltage and $q_{\text{cell,max}}, q_{\text{cell,exp}}$ are the maximum and exponential capacities.

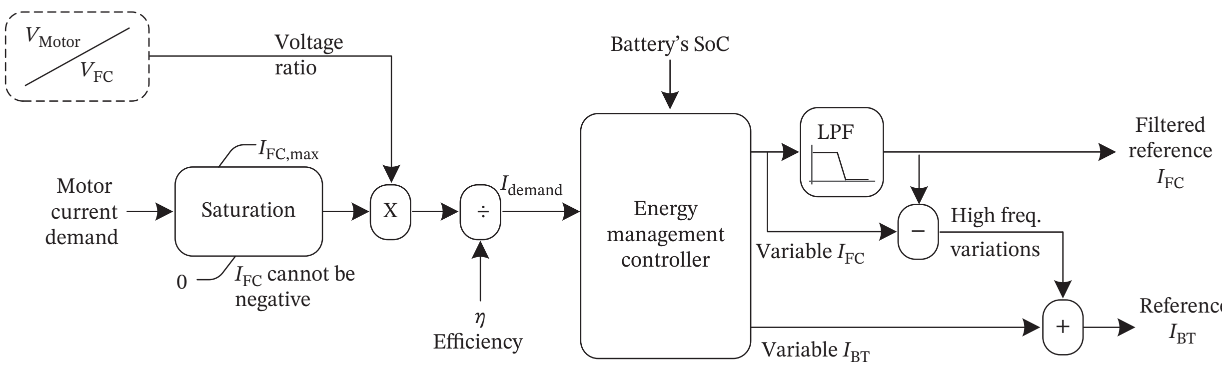

FIGURE 3 | DC–DC boost converter controller.

TABLE 3 | Cell configuration for 200 kWh battery [23].

Parameter	XALT 43 Ah high power cell	Multiply by	XALT XMP 76P high power pack	Multiply by	200 kWh for the battery
Energy (kWh)	0.16	48	7.636	27	206
Number of cells	1	(24s 2p)	48	(24s 2p) × (9s 3p) = 16s 6p	1296

TABLE 4 | Battery model parameters [23].

Parameter	Notation	Value
Cells in series	n_s	216
Cells in parallel	n_p	6
Nominal cell capacity	$q_{\mathrm{cap,cell,nom}}$	154,800 C
Maximum cell voltage	$v_{\mathrm{cell,max}}$	4.2 V
Nominal cell voltage	$v_{\mathrm{cell,nom}}$	3.7 V
Minimum cell voltage	$v_{\mathrm{cell,min}}$	3 V
Capacity-fade factor	$\sigma(t)$	(0,1)
Resistance-growth factor	$\gamma(t)$	≥ 1

At the pack level we include state-of-health (SoH) to account for aging via:

$$v_{\mathrm{pack}}(\mathrm{t}) = n_{\mathrm{s}}\mathrm{OCV}(\mathrm{SoC}(\mathrm{t})) - i_{\mathrm{BT}}(t)\underbrace{\gamma(t)R_0}_{R_{\mathrm{int}}(\mathrm{t})}, \tag{10}$$

$$\mathrm{SoC}(t) = -\frac{i_{\mathrm{BT}}(t)}{\underbrace{\sigma(t)Q_{\mathrm{pack},0}}_{Q_{\mathrm{pack}}(t)}}, Q_{\mathrm{pack}}(\mathrm{t})\sigma(t) = n_{\mathrm{p}}Q_{\mathrm{cell}}. \tag{11}$$

Here, R_0 is the beginning-of-life pack internal resistance and $Q_{pack,0}$ is the beginning-of-life pack charge capacity; SoH enters via the capacity-fade factor $\sigma(t)\varepsilon(0,1]$ and resistance-growth factor $\gamma(t) \geq 1$. The sign convention is $i_{BT} \geq 0$ for discharge. In this study, the pack operates between 85% and 35% SoC, giving around 100 kWh usable energy per trip; unless otherwise stated, $\sigma(0) = 1$, $\gamma(0) = 1$.

2.2.5 | Electric Drive Unit: (D) FC System (PEM)

The PEM FC stack (max net power 150 kW) provides most traction energy. The cell ideal voltage is given by the Nernst relation:

$$v_{\mathrm{ideal}} = v^0 + \frac{RT}{2F}\ln\left(\frac{p_{\mathrm{H_2}}p_{\mathrm{O_2}}^{0.5}}{p_{\mathrm{H_2O}}}\right), \tag{12}$$

where v^0 (v) denotes the standard cell voltage, R (J/[$\mathrm{K_{mol}}$]) the gas constant, T the temperature, F in C/mol Faraday's constant, and p the partial pressures of reactants/products [24].

Practical operation introduces three losses:

- Activation loss (low current densities):

$$\Delta V_{\mathrm{act}} = \frac{RT}{2\alpha F}\ln\left(\frac{i + i_n}{i_0}\right), \tag{13}$$

where i in A/m^2 denotes the current density drawn from the cell, i_n in A/m^2 the current density loss, i_0 in A/m^2 the exchange current density, and α the charge–transfer coefficient.

- Ohmic loss (ionic/electronic resistance):

$$\Delta v_{\mathrm{ohm}} = ir, \tag{14}$$

where r (Ω) is the area-specific resistance.

- Concentration loss (mass-transport limits) [20]:

$$\Delta v_{\mathrm{conc.}} = -\frac{RT}{2F}\ln\left(1 - \frac{i}{i_L}\right), \tag{15}$$

with i_L (A/m^2) the limiting current density.

The actual cell voltage is then,

$$v_{\mathrm{actual}} = v_{\mathrm{ideal}} - \Delta v_{act} - \Delta v_{\mathrm{ohm}} - \Delta v_{\mathrm{conc}}. \tag{16}$$

The stack voltage is $V_{\mathrm{FC}} = N_{\mathrm{cells}}v_{\mathrm{actual}}$ and stack power $P_{\mathrm{FC}} = V_{\mathrm{FC}}I_{\mathrm{FC}}$. Operational limits used throughout the simulations are $0 \leq i_{\mathrm{FC}} \leq i_{\mathrm{max}} = 450\mathrm{A}$ with start-up delay of 5 s. with a small current-slew filter (Figure 3). Unless otherwise stated, the desired operating point is $P_{\mathrm{FC}} = 70\,\mathrm{kW}$, which corresponds to $i_{\mathrm{FC,dOP}} = 178\mathrm{A}$ on the stack polarization curve (Figure 4). Key parameters are summarized in Table 5. Figure 4 shows efficiency and power characteristics.

3 | Model Implementation

To streamline the simulation process of the developed model, the coach bus route is scaled down by a factor of $\frac{1}{10}$ (Table 6. Figure 5

TABLE 5 | Fuel-cell parameters [18].

Parameter	Notation	Value
Number of cells in the stack	n_{cell}	526
Exchange current density (A/m^2)	i_0	15
Coefficient m (V)	m	3.0×10^{-4}
Coefficient n (A/m^2)	n	3.2×10^{-4}
Charge transfer coefficient	α	0.5
Current density loss (A/m^2)	i_n	0.22
Cathode side pressure (Pa)	p_{cath}	250,000

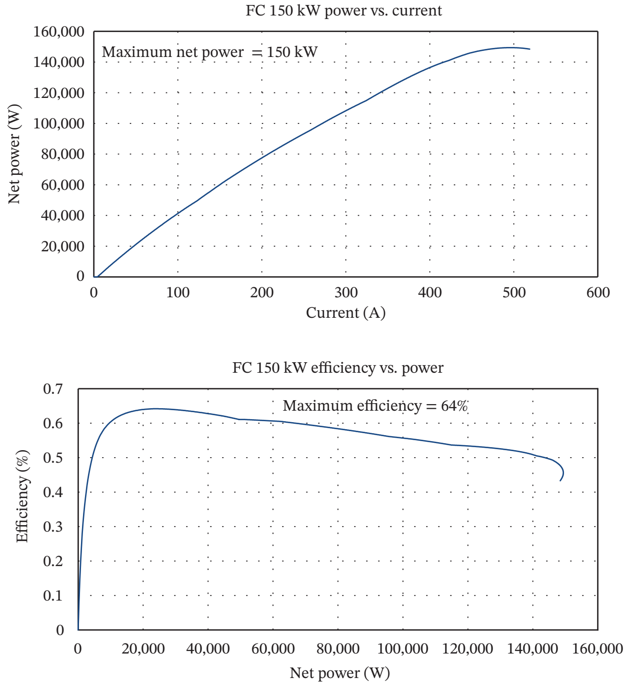

FIGURE 4 | Fuel-cell system efficiency and power curve.

TABLE 6 | Coach bus route vs. drive cycle for simulation.

Case	Distance (km)	Time (h)	max speed (km/h)	Average speed (km/h)
Coach bus route	650	8	100	80
Simulated drive cycle	65	0.8	100	80

depicts the resulting drive cycle, which is used extensively throughout the simulations. Figure 6 graphs the power profiles of the electric motor, battery, and FCs. The required motor power

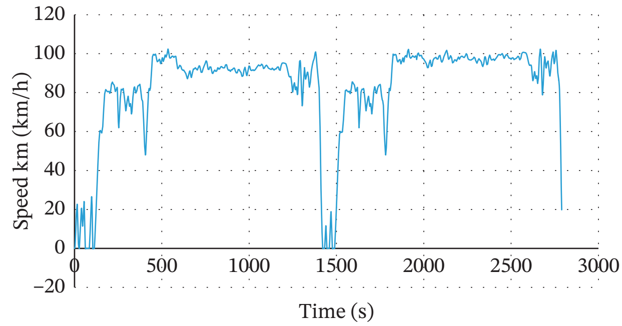

FIGURE 5 | Scaled drive cycle used in simulation (vehicle speed vs. time). This cycle forms the basis for the power flow results as shown in Figure 6.

is represented in orange color. The FC system, in green, supplies a constant power demand of 70 kW throughout the drive cycle. The battery, shown in blue, handles the peak power demands and recuperation, which effectively manages power fluctuations. The battery power can be simply defined as:

$$P_{\mathrm{BT}} = P_{\mathrm{Motor}} - P_{\mathrm{FC}}, \tag{17}$$

where P_{BT}, P_{Motor}, and P_{FC} are, respectively, the battery, motor, and FC power levels. The battery and the FC supply the required motor energy. During deceleration phases of the drive cycle, the electric machine operates as a generator and feeds energy back to the battery. In the results, this appears as negative battery power, for regenerative braking. The energy storage system (ESS) supplies the total energy to drive the FCHV, which can be written as:

$$E_{\mathrm{Total}} = E_{\mathrm{FC}} + E_{\mathrm{BT}}, \tag{18}$$

where E_{Total}, E_{FC}, and E_{BT} are the total supplied energy, FC energy, and battery energy. Table 7 summarizes the results of the energy analysis. The FCHV has a system-specific energy consumption of 0.95 kWh/km without considering the HVAC load. The total energy required by the FCHV for the distance of 650 km can be calculated as:

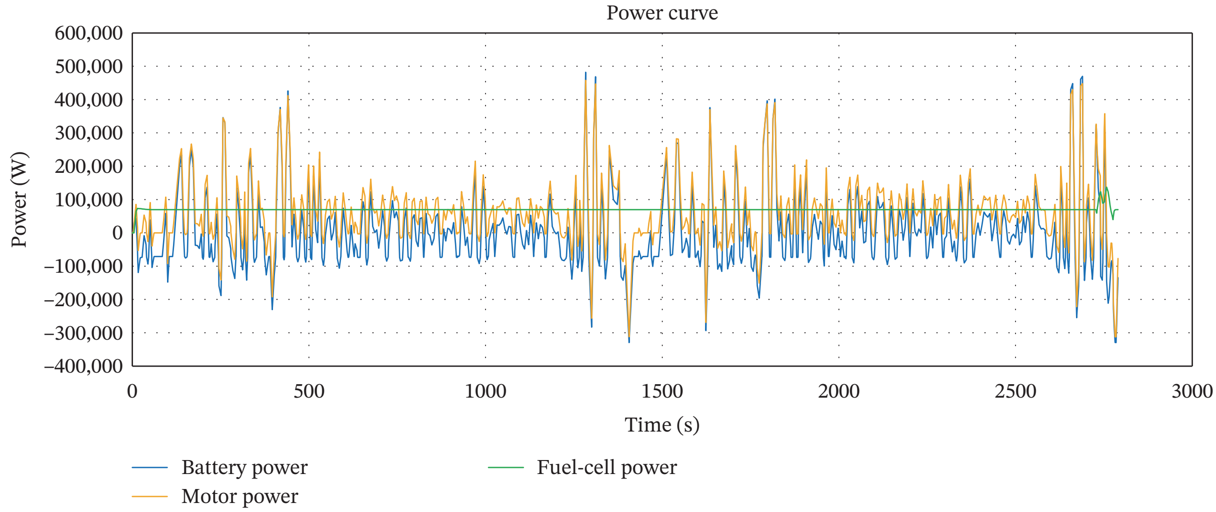

FIGURE 6 | Power profiles of motor, fuel-cell, and battery during the drive cycle of Figure 5. Positive battery power indicates discharge to support traction and negative battery power indicates regenerative braking.

TABLE 7 | Energy analysis.

Parameter	Value
Drive cycle distance	65 km
Drive cycle time	0.8 h/48 min/2880 s
Required motor electrical energy	50 kWh
Supplied fuel-cell energy	54 kWh
Supplied battery energy	8 kWh
Total energy supplied	62 kWh
Energy consumption	0.95 kWh/km (no HVAC Load)

$$E_{\text{Total},650} = D_{\text{Total}} E_{\text{km}} = 650\,\text{km} \times 0.95\frac{\text{kWh}}{\text{km}} = 618\,\text{kWh}, \tag{19}$$

where D_{Total} and E_{km} are the total travel distance and energy consumption per km. Hence, the total energy required by the FCHV is approximately 650 kWh, with an additional 32 kWh as backup, to travel the target distance of 650 km.

4 | Hybrid System Sizing

The hybrid system sizing determines the optimal size of the battery and FC system based on the target range, initial cost, operating cost, operating conditions, and system life.

4.1 | Battery Sizing

The minimum size of the battery takes into consideration the power requirement and desired lifespan. The maximum power needed from the battery to operate the electric motor can be calculated as follows:

$$P_{\text{BT,max}} = \frac{P_{\text{Motor,max}}\,(450\,\text{kW})}{\eta_{\text{Inverter}}(0.92) \times \eta_{\text{DC/DC}}(0.92) \times \text{Other losses}\,(0.95)} = 560\,\text{kW}, \tag{20}$$

where $P_{\text{Motor,max}}$ is the maximum motor power, η_{Inverter} the inverter efficiency, and $\eta_{\text{DC-DC}}$ the DC–DC converter efficiency.

The battery pack can be operated at the maximum C-rate up to 5.5C [23]. However, operating the battery at higher C-rates causes a larger voltage drop and faster degradation, which reduces battery life. To improve performance and lifespan, the pack is therefore limited to ≤ 3C. The minimum battery size considering operation below 3C is as follows:

$$S_{\text{BT,min}} = \frac{P_{\text{BT,max}}\,(560\,\text{kW})}{C_{\text{Nominal}}(3\text{C})} = 190\,\text{kWh}, \tag{21}$$

where $S_{\text{BT,min}}$ is the minimum battery size, $P_{\text{BT,max}}$ the maximum battery power, and C_{Nominal} the nominal C rate of the battery.

From Equations (20) and (21), the power-driven minimum energy requirement decreases with higher C-rate capability: 5C → approximately 112 kWh, 10C → approximately 56 kWh. In our plug-in operation, however, the battery delivers approximately 100 kWh usable per trip (85%→35% SoC on a 200 kWh pack). Thus, the energy requirement dominates, and the selected 200 kWh pack remains unchanged even with higher-C technology. While higher-C cells would reduce relative stress, they typically exhibit lower Wh/kg and higher €/kWh, which offers no range or hydrogen benefit for this mission.

The minimum size is also constrained by aging. With the SoH model $Q_{\text{pack}}(t) = \sigma(t) Q_{\text{pack},0}$ and $R_{\text{int}}(t) = \gamma(t) R_0$, capacity fade ($\sigma$) reduces usable energy, while resistance growth (γ) increases voltage sag and limits peak power. By selecting a 200 kWh pack operated between 85% and 35% SoC, robustness is maintained against expected aging, preserving both the approximately 100 kWh energy swing and peak-power headroom relative to the 3C design point.

4.2 | FC System Sizing

Figure 7 analyzes the efficiency versus power curve for various FC system sizes ranging from 70 to 200 kW. Based on the energy requirement (Section 3), the hybrid system requires a stable power output from the FC in the 60–80 kW range. It is determined that a 150 kW FC system would operate with better efficiency (0.6) and within a healthier operating range than smaller ones. Additionally, the 150 kW FC system has an operating voltage range of 400–500 V, which matches the DC bus nominal voltage of 750 V. This voltage choice reduces the boost converter effort to elevate the voltage and increase its efficiency compared to smaller FC systems. Smaller FC systems would incur higher costs per kilowatt of power and require more space for additional components like batteries or fuel tanks.

4.3 | Optimal Size of Battery and FC Hybrid System

Figure 8 plots the total cost over the different hybrid system sizes to determine the optimal size of the hybrid system based on the total cost of ownership (TCO). The total cost includes the initial hardware cost and the operating costs of the battery and FC system including hydrogen tanks. Figure 8 also shows the minimum battery size, the weight, and volume limits. The optimal hybrid system size includes a 200-kWh high-power battery and a 150-kW FC system with a constant net power of 70 kW. This selection accounts for factors such as initial cost, operating cost, TCO, weight/volume limits, and minimum battery size.

5 | EMS

The EMS defines the hybrid system's function based on the load condition. The performance of the system largely depends on the EMS. Therefore, it is important to have an efficient EMS for better performance, which includes optimal system life. The objectives outlined for the EMS in this work are as follows:

- Improve the overall operational efficiency of the system.
- Maintain the FC stack within its maximum efficiency (ME) range.

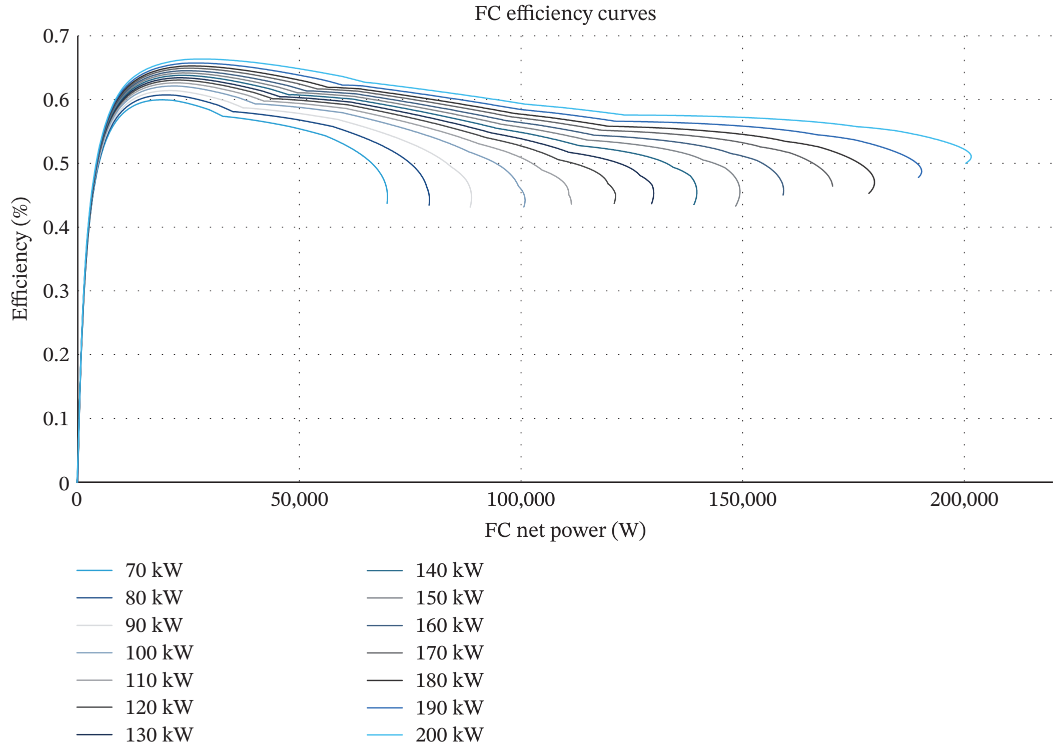

FIGURE 7 | Efficiency vs. power curve for different fuel-cell sizes.

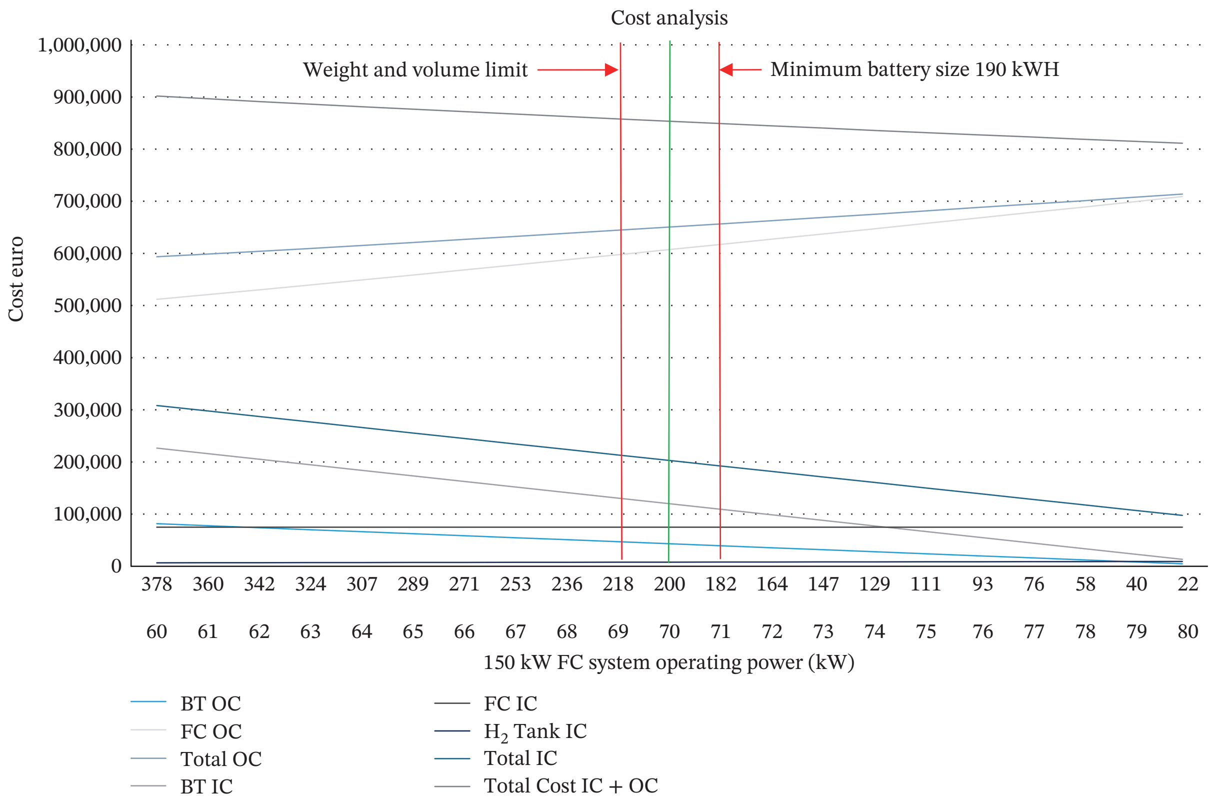

FIGURE 8 | Cost analysis of a hybrid system.

- Provide a consistent and stable power request to the FC system.
- Avoid multiple start–stop cycles of the FC system.
- Ensure the battery discharges to the desired SoC by the end of the drive cycle.
- Optimize battery operation within the efficient SoC range for extended durations.
- Reduce degradation of the FC system and battery to increase the system's overall lifetime.
- Minimize fuel consumption.

The optimization method is a multiobjective approach to design the hybrid ESS for a long-range electric coach bus. The key objectives are to minimize cost, maximize range, optimize efficiency, and ensure system longevity. The optimization process includes the following steps:

1. Objectives
2. System constraints
   - Battery and FC power must meet demand.
   - Weight and volume must fit within the bus's available space.
3. Hybrid system selection
   - Battery: 200 kWh (optimized for peak demand and optimal C-rate).
   - FC: 150 kW (ensures efficiency and stable power).
4. Optimization algorithm: genetic algorithm
   - Selection: evaluate solutions based on an objective function.
   - Crossover: combine solutions to generate new ones.
   - Mutation: random adjustments to explore other solutions.
   - Termination: repeat until convergence.

5.1 | Bounded-Load-Following Control Strategy (BLFCS)

The BLFCS is commonly used as a performance benchmark and has been implemented in the literature [25–27]. The FC system operates under the BLFCS, which optimizes performance within the efficiency and power limits. This strategy ensures safe operation within the region defined by the ME point and the maximum-power point (MPP) [28]. Figure 9 illustrates the operation of the plug-in hybrid electric vehicle under the BLFCS in two different operating modes: charge-depleting mode and charge-sustaining mode.

The charge-depleting mode occurs when the vehicle is solely powered by the battery, also known as the battery mode. During this mode, the battery discharges from its maximum charge (SoC_{max}) to the desired one ($SoC_{desired}$). The charge sustaining mode involves the simultaneous operation of both the battery and the FC system, also called the hybrid mode. In this mode, they work together to maintain the desired minimum SoC (SoC_{min}) of the battery until the end of the drive cycle. Upon reaching this

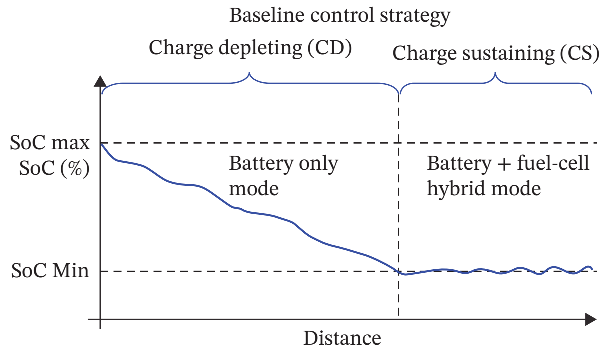

FIGURE 9 | BLFCS operating modes [28].

specified level of charge, the FC activates. Therefore, the criterion for FC activation is expressed as $\mathrm{SoC}(t) \leq \mathrm{SoC}_{desired}$, where $\mathrm{SoC}(t)$ represents the battery's instantaneous SoC over time. During the charge-sustaining phase, the power request to the FC is determined by:

$$i_{FC} = i_{cmd} + \alpha(\mathrm{SoC}_{desired} - \mathrm{SoC}(t)), \forall\, i_{cmd} \leq i_{FC}, \tag{22}$$

where i_{FC} denotes the current demand from the FC system, i_{cmd} signifies the motor current, and α is a constant that adjusts the FC current request based on the SoC disparity. If i_{cmd} exceeds i_{FC}, the battery supplies the excess power. Conversely, the battery absorbs recuperation power during regenerative braking, marked by negative motor currents.

5.1.1 | Bounded-Load-Following Control Algorithm

Equation (23) outlines the pseudocode within the controller for the BLFCS. Initially, a 5-s duration is allocated for the startup of the FC system. In this algorithm, SoC denotes the instantaneous state of charge of the battery.

$$\begin{array}{ll}
\textbf{IF} & \textbf{time} \leq 5 \\
\quad - & i_{FC} = 0 \\
\quad - & i_{BT} = i_{cmd} \\
\multicolumn{2}{l}{\textbf{ELSEIF SoC} \geq \textbf{SoC}_{\textbf{minD}}} \\
\quad - & i_{FC} = 0 \\
\quad - & i_{BT} = i_{cmd} \\
\multicolumn{2}{l}{\textbf{ELSEIF}\ \ \textbf{SoC}_{\textbf{minD}} \geq \textbf{SoC} \geq \ \textbf{SoC}_{\textbf{min0}}} \\
\quad - & i_{FC} = i_{FCME} + \alpha\,(\mathrm{SoC}_{minD} - \mathrm{SoC}) \\
\quad - & i_{BT} = i_{cmd} - i_{FC} \\
\multicolumn{2}{l}{\textbf{ELSEIF SoC} \leq \textbf{SoC}_{\textbf{min0}}} \\
\quad - & i_{FC} = i_{max} \\
\quad - & i_{BT} = i_{cmd} - i_{FC} \\
\multicolumn{2}{l}{\textbf{ELSE}} \\
\quad - & i_{FC} = 0 \\
\quad - & i_{BT} = 0.
\end{array} \tag{23}$$

Additionally, SoC_{minD} represents the desired minimum SoC of the battery, while SoC_{min0} indicates the minimum SoC threshold. If the battery falls below SoC_{min0}, the FC system operates at the MPP. $i_{FC_{ME}}$ corresponds to the FC current at the ME point, and i_{max} signifies the FC current at the MPP. The parameter α adjusts the FC demand current based on the SoC condition. The precise value of α is determined through a trial-and-error method, based on observations of

TABLE 8 | BLFCS control parameters.

Parameter	Value
i_{max}	450 A
$i_{fc-Effmax}$	80 A
SoC_{min0}	30%
SoC_{minD}	35%
α	75,000

the battery SoC. Table 8 lists the specific parameter values used in the controller for this strategy. The limitations of the BLFCS are:

- Lack of control over the operating point of the FC.
- The FC may work in the low-efficiency region to maintain desired SoC_{minD} of the battery.
- High fuel consumption.
- The fluctuating load may increase the degradation rate of FC and battery system and ultimately reduce life time.

5.2 | EPCS

To solve the limitations of the BLFCS, the EPCS is implemented in the controller. The EPCS relies on accurately predicting the total energy required by a coach bus to complete a specific drive cycle or route. It then optimally depletes the energy stored in the onboard storage system (FC and battery) to allow them to operate in the optimal region and achieve the desired goals [27]. The total energy required comes from simulating the drive cycle or analyzing historical data from real-time trips. The goal is to draw the net power from the FC system in a way that maximizes its efficiency. The EPCS activates the FC system earlier, before the battery SoC reaches the desired SoC, based on energy predictions [27].

Given the target drive cycle of duration T_{cycle}, the total traction energy required is estimated from the drive-cycle (or historical) data. The net FC energy needed is as follows:

$$E_{FC,predicted} = E_{total} - E_{BT,useful}, \tag{24}$$

where E_{total} is the total estimated energy required from the energy systems, with the battery's useful energy as follows:

$$E_{BT,useful} = (SoC_{max} - SoC_{desired})\,\eta_{DC-DC}\,\eta_{BT}\,(200\,\text{kWh}), \tag{25}$$

With the desired constant FC operating power $P_{FC,dOP} = 70\,\text{kW}$ (from Figure 4), the turn-on time is:

$$T_{FC;start} = T_{cycle} - \left[\frac{E_{FC,predicted}}{P_{FC;dOP}}\right], \tag{26}$$

where $T_{FC;start}$ is the time when FC system turns on, $E_{FC;predicted}$ is the net energy required from FC system, and $P_{FC;dOP}$ is the FC power at the desired operating point (parameters and the 178 A set-point corresponding to $P_{FC;dOP}$ are taken from Figure 4 and Table 8).

Figure 10 demonstrates the operation of the EPCS, which turns on the FC system before the battery reaches the desired SoC and supplies constant power to the electric drive until the end of the drive cycle [27]. Since the BLFCS turns the FC system on as soon as the desired battery SoC is reached, the FC system must operate in a high-power zone which reduces the efficiency of the FC system. Also, the FC system operates with fluctuating power which is not desirable for the longevity of the system. However, in case of EPCS, the energy management system estimates the required energy ahead of time to ensure that the FC operates at optimum efficiency, and it does not face any fluctuating power. Nevertheless, the predicted energy may not be completely

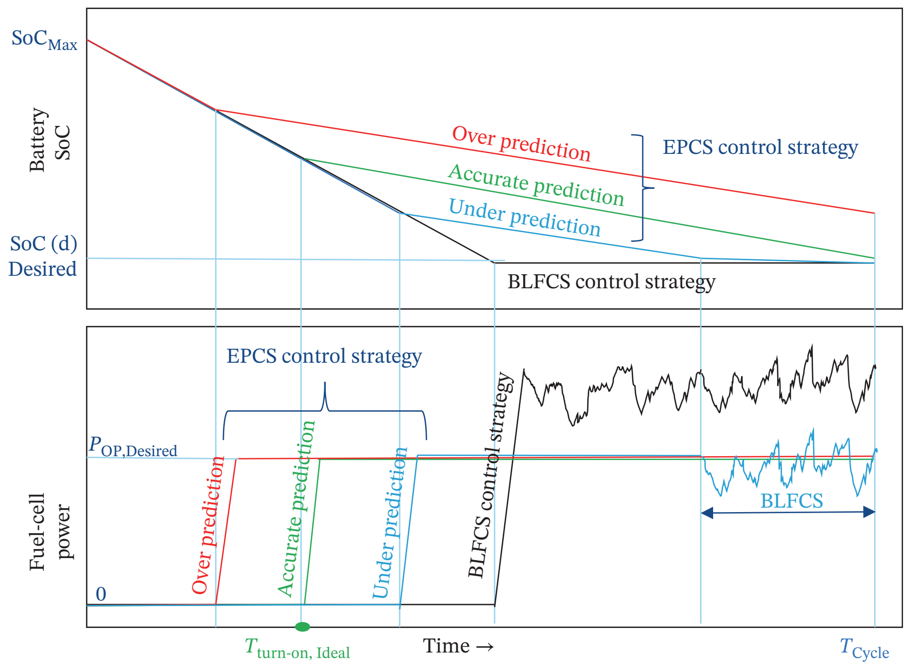

FIGURE 10 | Energy-prediction-based control strategy (EPCS) cases [27].

accurate all the time. Hence, depending on the prediction accuracy, three different scenarios can be foreseen.

Equation (27) explains the controller conditions for the EPCS. i_{cmd} is defined as the motor current request mapped to the DC bus, and SoC the battery state of charge. With start-up delay of 5 s and current limits $0 < i\text{FC} < i\text{max}$, the FC current is commanded as:

$$i_{\text{FC}}(t) = \begin{cases} 0, \quad t \le T_{FC,\text{start}} \text{ or } t \le 5 \\ i_{\text{FC};dOP}, \quad t \ge T_{\text{FC,start}} \wedge \text{SoC} \ge \text{SoC}_{\text{desired}} \\ i_{\text{FC},ME} + \alpha(\text{SoC}_{\text{desired}} - \text{SoC}), \quad \text{SoC}_{\text{min0}} \le \text{SoC} \le \text{SoC}_{\text{desired}} \\ i_{\text{max}}, \quad \text{SoC} \le \text{SoC}_{\text{min0}} \end{cases}, \tag{27}$$

saturated to $[0, i_{\text{max}}]$. The battery current follows $i_{BT} = i_{\text{cmd}} - i_{FC}$.

The controller acts with the power balance $P_{\text{BT}} = P_{\text{Motor}} - P_{\text{FC}}$ and the SoC dynamics $\text{SoC} = -\frac{i_{\text{BT}}}{Q_{\text{pack}}}$ defined earlier; limits i_{max} and $i_{\text{FC, ME}}$ are given in Table 8. Under this law, the FC provides steady power near its high-efficiency region while the battery covers transients. Figure 10 details accurate/over-/under-prediction cases.

Depending on the accuracy of the energy prediction, there are three different cases of the EPCS called accurate prediction, over-prediction, and under-prediction (Figure 10).

Case 1: Accurate prediction: E_{FC}, predicted $= E_{\text{FC}}$, net accurate

An accurate prediction is the ideal case of the EPCS. In the case of an accurate prediction, the FC system will start at the ideal turn-on time and will supply the constant desired power until the end of the drive cycle. Also, the battery SoC reaches the desired value exactly at the end of the drive cycle.

Case 2: Over-prediction: E_{FC}, predicted $> E_{\text{FC}}$, net accurate

In this case, the FC system starts earlier than the ideal turn-on time and operates with the constant desired power until the end of the drive cycle, but the battery SoC at the end of the drive cycle is higher than the desired SoC, which is not an ideal case for the efficiency of the plug-in hybrid vehicle.

Case 3: Under-prediction: E_{FC}, predicted $< E_{\text{FC}}$, net accurate

In this case, the FC system starts later than the ideal turn-on time and supplies the constant desired power until the battery SoC reaches the desired SoC. Afterward, the FC system must also supply fluctuating power similar to the BLFCS, until the end of the drive cycle.

Accurate energy predictions are key to optimizing FCHV operation. The energy-prediction-based control system differentiates between accurate, over, and under predictions, which affect FC activation and battery management.

6 | Results

6.1 | Comparison of Different Control Strategies

Figure 11 presents the comparison of results for both strategies. Three graphs represent the battery SoC, FC net power, and FC system efficiency over the drive cycle time. The accurate prediction case is

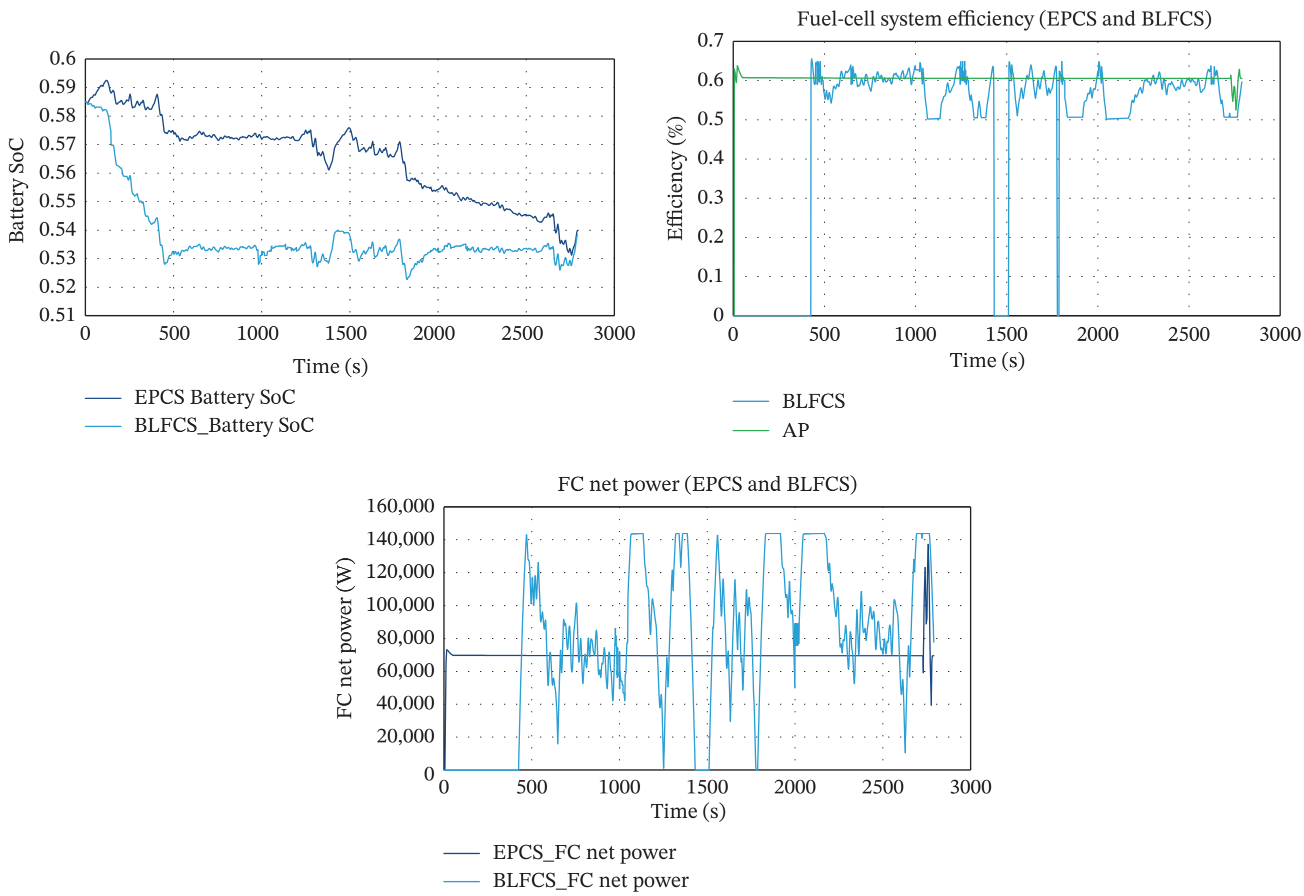

FIGURE 11 | Results comparison–bounded-load-following and energy-prediction-based control strategies.

Parameter	BLFCS	EPCS
Average efficiency	54%	60%
Hydrogen consumption	3.6 kg	3 kg
Fuel saving	—	16.7%

TABLE 9 | EPCS vs. BLFCS results.

considered in this result. In the EPCS, the battery SoC gradually decreases and reaches the desired SoC at the end of the drive cycle. This allows the battery to operate in the optimal operating region for most of the drive cycle, which is beneficial for the battery lifetime. In contrast, the BLFCS results in a drastic reduction of battery SoC at the beginning of the drive cycle, followed by maintaining the desired SoC until the end of the drive cycle.

In the EPCS, the FC system starts at the beginning of the drive cycle and consistently delivers a power of 70 kW until the end of the drive cycle. On the other hand, the BLFCS initiates the FC system at a later stage, as soon as the desired battery SoC is reached and then provides highly fluctuating power to maintain the desired SoC. Fluctuating power demand and frequent start/stops of the FC system cause higher degradation of the FC stack. These should be avoided to prolong the FC system's lifespan. As depicted in the efficiency curve, the EPCS ensures that the FC system maintains consistently high efficiency of 0.6 across the entire drive cycle. In contrast, the BLFCS operates the FC system within lower efficiency regions, primarily to meet the demands of power peaks. Table 9 compares the EPCS and the BLFCS. The EPCS achieves an average efficiency of 60%, while the BLFCS yields 54%. In terms of hydrogen consumption, the BLFCS requires 3.6 kg and only 3 kg for the EPCS, which indicates a fuel-saving advantage of 16.7% for the EPCS over the BLFCS.

These results confirm that the proposed EPCS not only reduces hydrogen consumption by 16.7% compared to BLFCS but also enables daily autonomy of 650 km with approximately equal to 30 kg of hydrogen, compared to approximately equal to 36 kg required by BLFCS.

6.2 | EPCS for Different Prediction Cases

Three different energy-prediction cases are considered to analyze the performance of the EPCS: under-prediction, accurate prediction, and over-prediction. In the under-prediction case, the net energy is 5% less than the accurate prediction, whereas in the over-prediction case, the net energy is 5% more. Figure 12 shows the performance of the EPCS for all three different cases.

The performance of the accurate prediction and under-prediction cases is the same because the FC system starts at the beginning of the cycle in both cases. It is designed to start at the beginning of the drive cycle for the target range of 650 km. However, for different driving distances, the start time of the FC system may vary. In the under-prediction case, the FC system starts later, which causes the system to operate with a fluctuating load (higher power) at the end to maintain the desired SoC.

6.3 | Energy-Prediction-Based Control for Different Distances

Although the system is designed for a target range of 650 km, this section analyzes the system's performance also for 500 and 800 km. Figure 13 illustrates the scaling down of the drive cycle for each respective travel distance by a factor of 1/10. Figure 14 demonstrates the performance of EPCS for these different travel distances.

For a total travel distance of less than 650 km, the FC system can operate with a constant power throughout the drive cycle. However, for travel distances exceeding 650 km, even if the FC system starts at the beginning of the cycle, it must cope with a fluctuating load (higher power) after the first 650 km. Up to 650 km, the battery SoC reaches the desired level at the end of the drive cycle. However, for distances beyond 650 km, the system maintains the desired SoC after reaching 650 km by supplying fluctuating power through the FC system.

6.4 | Results Comparison

Figure 15 presents a comparison of the results for five different cases of the EPCS: (i) −5% and (ii) −10% under-prediction, (iii) accurate prediction, and (iv) +5% and (v) +10% over-prediction, across three different travel distances (500, 650, and 800 km). The performance of the BLFCS serves as the benchmark for comparison. The analysis includes a comparison of total hydrogen consumption, percentage of fuel savings, average efficiency of the FC system, and the battery SoC at the end of the drive cycle for each scenario.

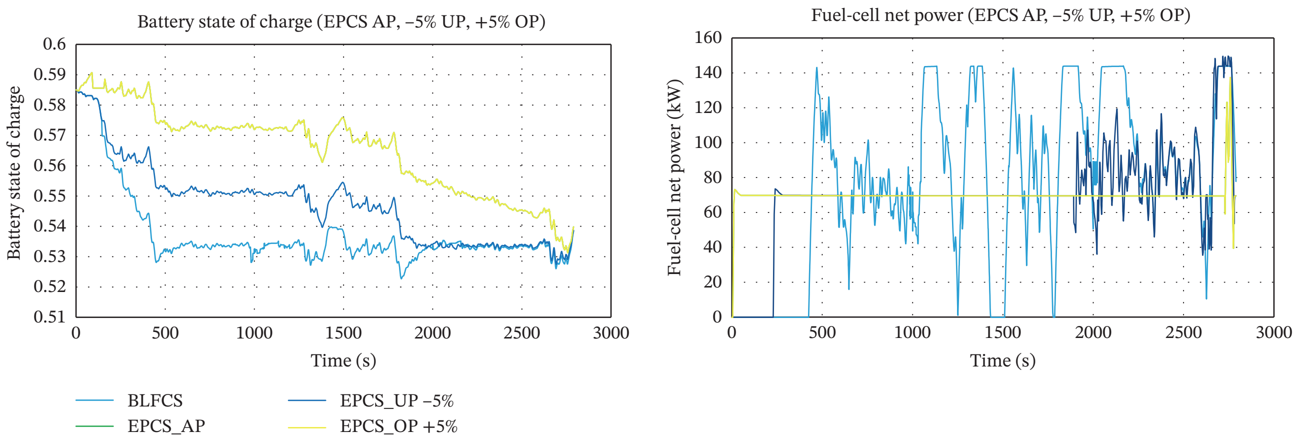

FIGURE 12 | Energy-prediction-based control strategy results for different prediction cases.

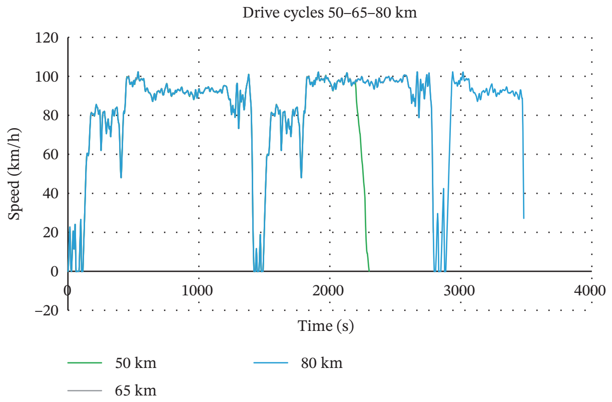

FIGURE 13 | Drive cycle for different travel distances.

The hydrogen consumption for the BLFCS is the highest among all the scenarios, while the hydrogen consumption or percentage of fuel savings for the EPCS with accurate prediction is the lowest overall. The fuel-saving for the under-prediction cases decrease as the percentage of the under-prediction increases. For travel distance more than 650 km, the fuel-saving of the EPCS for over-predictions are the same as for accurate prediction, as the FC system starts at the beginning of the drive cycle. However, for distances less than 650 km, the fuel-saving for over prediction decreases as the percentage of over prediction value increases. Additionally, the final SoC of the battery remains higher than the desired SoC, which is not ideal for plug-in hybrid vehicles. Although it is acceptable, the additional charge to the battery is supplied by the FC system instead of grid electricity, which increases the operating cost of the vehicle. Charging the battery

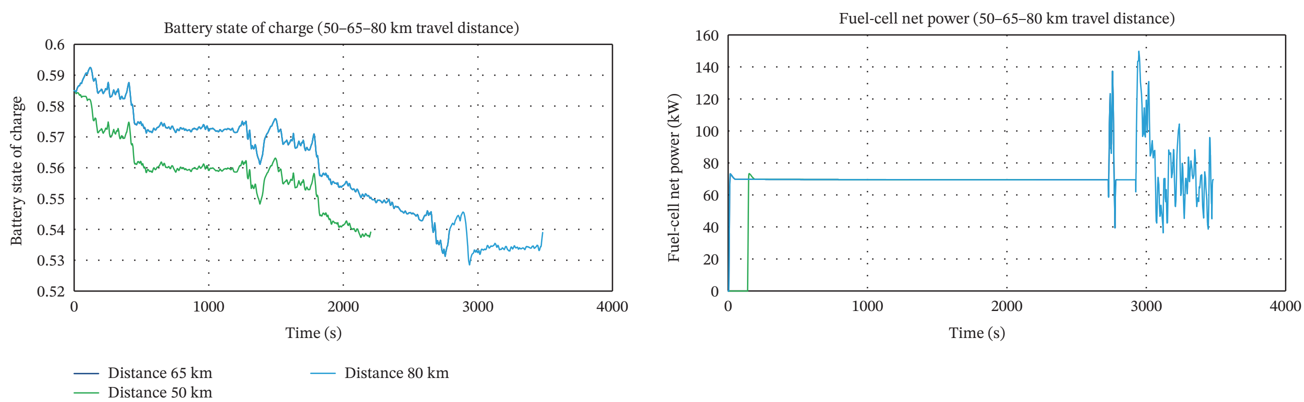

FIGURE 14 | Energy-prediction-based control strategy performance for different travel distances.

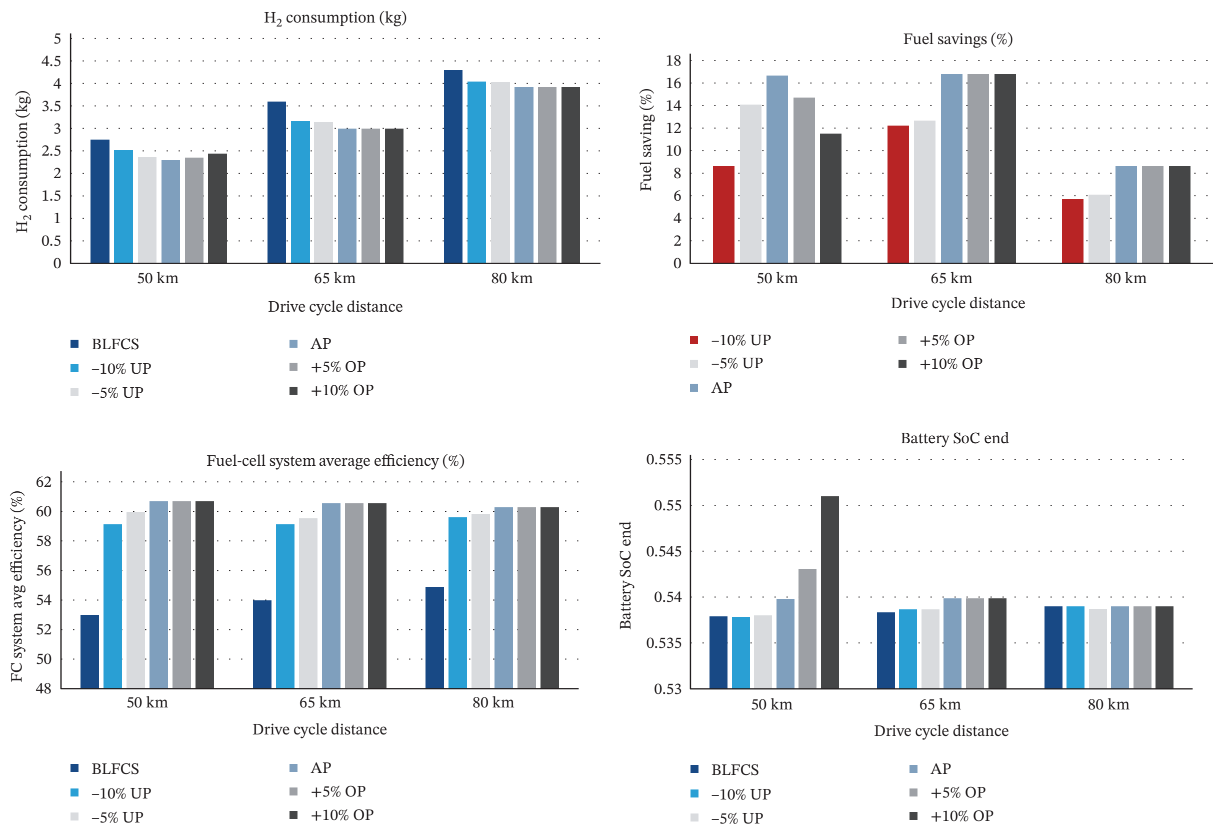

FIGURE 15 | Results comparison.

through the FC system is 2.5-times more expensive than charging it from the grid. Grid electricity costs as little as € 0.12/kWh, while charging through the FC system costs some € 0.3/kWh [29].

6.5 | TCO Comparison

This section compares the TCO of four types of coach buses: FCEV, FCHV, BEV, and a conventional diesel bus. Figure 16 illustrates the overall TCO composition, while Table 10 presents the powertrain sizes and fuel costs. The coach bus is assumed to travel 650 km per day, and over 12 years of operation the total mileage is 2.34 million km, reflecting intensive usage.

To evaluate the impact of Li-ion price trends on TCO, the battery pack cost is defined as c_{batt} ($€$/ kWh). For a vehicle with pack size E_{pack} and N_{repl} replacements, the first-order TCO variation due to a price change Δc_{batt} is:

$$\Delta \text{TCO} = \left(1 + N_{\text{repl}}\right) E_{\text{pack}} \Delta c_{\text{batt}}. \tag{28}$$

Using Table 10 values—BEV 1000 kWh, FCHV 200 kWh, and FCEV 70 kWh—a €100/kWh price decrease reduces TCO by roughly € 100 k, € 20 k, and € 7 k, respectively. These reductions double if one mid-life replacement is assumed. Thus, falling battery prices most strongly improve BEV economics, moderately affect FCHV, and slightly influence FCEV. Fuel costs remain the dominant driver for FCEV and FCHV.

Among the four bus types, the conventional diesel bus has the lowest initial cost but the highest overall TCO due to fuel expenses. The BEV has the lowest operating cost but the highest upfront investment, almost double that of the diesel bus. The FCEV and FCHV fall between these extremes. Both incur similar maintenance and replacement costs, but the FCHV TCO is lower due to partial reliance on grid electricity, covering about 100 kWh per trip.

In the BEV case, charging time increases for longer routes and may require additional infrastructure. By contrast, the FCHV combines a 150 kW FC system with grid charging, which lowers hydrogen demand and improves cost-effectiveness. Overall, the TCO analysis shows that FCHV offers lower operational costs than both BEVs and FCEVs, mainly due to grid electricity usage, while ongoing battery price declines favor BEVs most and FCHVs moderately.

6.6 | Weight and Volume Comparison

As shown in Figure 17, the weight of the powertrain system for the conventional diesel engine bus is the lowest among the four types, while the weight and volume of the powertrain system plus ESS are highest for the BEV type. The weight of the FCEV and FCHV types falls between the BEV and conventional bus powertrain systems, while the volumes of FCEV, FCHV, and conventional bus powertrain systems are all within a similar range.

In the case of the BEV, the inclusion of the ESS results in an increase in weight of up to 3.5 tons, which may necessitate improved axle strength and suspension. Additionally, there is an increase in volume of up to 2 m^3, which could be accommodated by reducing 2–4 passenger seats or adjusting the luggage compartment. It is important to note that the increase in weight by 3 tons has an impact on the required energy and performance of the BEV.

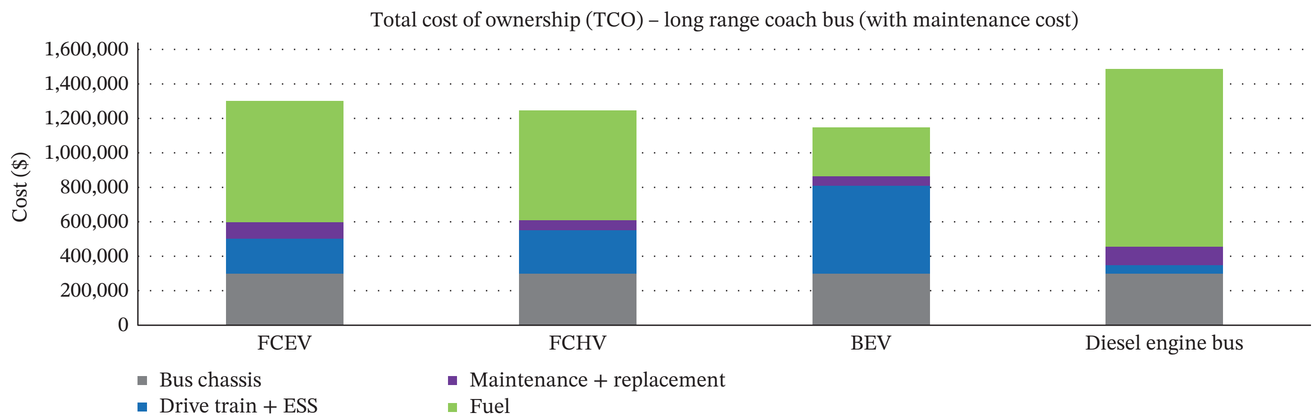

FIGURE 16 | TCO comparison [30–33].

TABLE 10 | Powertrain sizes, energy/fuel consumption, and unit-cost assumptions used in TCO [29].

Vehicle	Powertrain sizes	Energy/fuel consumption used	Unit prices
FCEV	FC 200 kW; BT 70 kWh (HP)	H_2: kg/100 km	€/kg
FCHV	FC 150 kW; BT 200 kWh (HP)	H_2: 4.6 kg/100 km (EPCS: 3.0 kg per 65 km); grid battery: 0.08–0.10 kWh/km (8 kWh per 65 km)	H_2 €/kg, electricity: € 0.12/kWh
BEV	BT 1000 kWh (HE)	Grid energy: e_{BEV} kWh/km	€ 0.12/kWh
Diesel bus	—	Fuel: f_{diesel} 1/100 km	€/1

Note: $\text{FCEV}_{\text{cost}} = \text{cost}(H_2)(\text{kg/km}) = €0.3/\text{kg}$; $\text{FCHV}_{\text{cost}} = 0.046 \times \text{cost}(H_2) + \text{Electricity cost} \times (E_{\text{grid,km}}) = €\,0.25/\text{kg}$; $\text{BEV}_{\text{cost}} = \text{Electricity cost} \times e_{\text{EBV}} = €\,0.12/\text{kg}$; $\text{Diesel bus}_{\text{cost}} = \text{Diesel cost} \times \frac{f_{\text{diesel}}}{100} = €\,0.44/\text{kg}$.

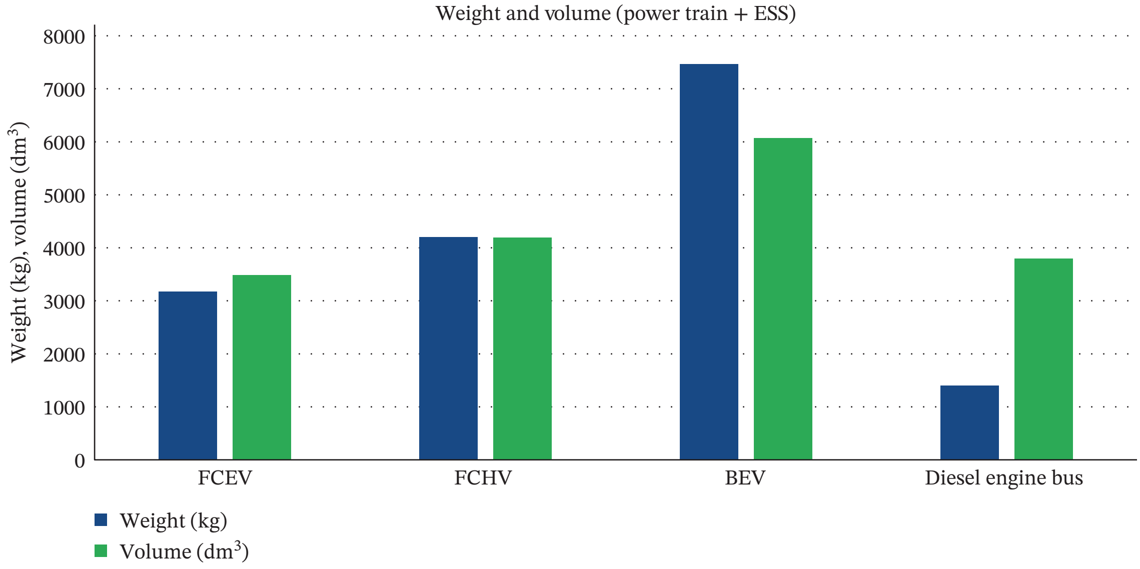

FIGURE 17 | Weight and volume comparison (powertrain + energy storage system) [25, 27, 30, 31] .

6.7 | Environmental Impact (CO_{2e})

We present well-to-wheel (WTW) greenhouse-gas emissions per kilometer for the four cases shown in Figure 16, where WTW includes both upstream fuel production and vehicle operation. The emission factors are defined as EF_{el} in $kgCO_{2e}/kWh$ for grid electricity, EF_{H_2} in $kgCO_{2e}/kg$ for hydrogen, and EF_{diesel} in $kgCO_{2e}/L$ for diesel fuel. Using the consumptions established in this study, the per-km emissions are as follows:

FCHV (plug-in):

$$CO_{2e_{FCHV}} = \underbrace{0.046}_{H_2\ kg/km\ (0.3\ kg/65\ km)} EF_{H_2} + \underbrace{0.123}_{kWh/km\ (8\ kWh/65\ km)} EF_{el}, \tag{29}$$

with hydrogen use of 0.3 kg/65 km and grid electricity use of 8 kWh 65 km (from Tables 9 and 8).

BEV:

$$CO_{2e_{BEV}} = e_{EBV} EF_{el}, \tag{30}$$

where e_{EBV} is the traction energy per km. Using Table 10 (fuel-cost line € 0.12 /km and the tariff € 0.12 /kWh as used in Sec. 6.4), $e_{EBV} \approx 1\,kWh/km$.

FCEV:

$$CO_{2e_{FCEV}} = h_{FCEV} EF_{H_2}, \tag{31}$$

where h_{FCEV} is the hydrogen use per km from the FCEV case (same route/vehicle).

Diesel:

$$CO_{2e_{Diesel}} = f_{diesel}/100 EF_{diesel}, \tag{32}$$

where f_{diesel} is the diesel consumption in L/100 km (Table 10).

7 | Conclusion

Although BEVs suit urban routes, their limited range constrains long-haul use. To overcome this limitation, we designed and optimized a plug-in FC hybrid coach bus integrating a 200-kWh battery and a 150-kW FC system. The proposed EPCS achieved 16.7% fuel savings and increased the FC system efficiency from 54% to 60%, compared to conventional bounded-load-following control. The system maintains the battery SoC within its safe operating range and extends the lifetime of both battery and FC. Techno-economic analysis confirmed that the FCHV achieves a 650 km driving range and offers a lower TCO and environmental footprint than both stand-alone BEVs and FCEVs. The optimization using a genetic algorithm further improved system sizing and performance beyond linear programming, particle swarm optimization, and simulated annealing. Overall, the hybrid coach bus concept balances range, cost, and environmental impact to provide a practical pathway for long-distance public transportation, where BEVs alone remain insufficient.

Funding

Open Access funding enabled and organized by Projekt DEAL.

Conflicts of Interest

The authors declare no conflicts of interest.

Data Availability Statement

The data that support the findings of this study are available from the corresponding author upon reasonable request.

References

1. H. Deng, Y. Zhang, R. Fang, and Z. Pei, "Study on Fuel Cell Vehicle Power System Selection and Simulation," in *2019 IEEE 4th Advanced Information Technology, Electronic and Automation Control Conference (IAEAC)*, (IEEE, 2019): 2382–2385.

2. J. D. Colgan, "The International Energy Agency: Challenges for the 21st Century," GPPi Energy Policy Paper (2009).

3. N. Tashakor, P. Pourhadi, M. Bayati, M. H. Samimi, J. Fang, and S. M. Goetz, "Modular Reconfigurable Mixed Battery System With Heterogeneous Modules," in *IEEE Transactions on Transportation Electrification*, (Early Access, 2024).

4. S. Rivera, S. Kouro, S. Vazquez, S. M. Goetz, R. Lizana, and E. Romero-Cadaval, "Electric Vehicle Charging Infrastructure: From Grid to Battery," *IEEE Industrial Electronics Magazine* 15, no. 2 (2021): 37–51.

5. M. S. Khan, I. Ahmad, and F. Z. Ul Abideen, "Output Voltage Regulation of FC-UC Based Hybrid Electric Vehicle Using Integral Backstepping Control," *IEEE Access* 7 (2019): 65693–65702.

6. N. Tashakor, B. Arabsalmanabadi, F. Naseri, and S. Goetz, "Low-Cost Parameter Estimation Approach for Modular Converters and Reconfigurable Battery Systems Using Dual Kalman Filter," *IEEE Transactions on Power Electronics* 37, no. 6 (2022): 6323–6334.

7. T. Rudolf, T. Schurmann, S. Schwab, and S. Hohmann, "Toward Holistic Energy Management Strategies for Fuel Cell Hybrid Electric Vehicles in Heavy-Duty Applications," *Proceedings of the IEEE* 109, no. 6 (2021): 1094–1114.

8. F. Odeim, J. Roes, and A. Heinzel, "Power Management Optimization of a Fuel-Cell/Battery/Supercapacitor Hybrid System for Transit Bus Applications," *IEEE Transactions on Vehicular Technology* 65, no. 7 (2016): 5783–5788.

9. X. Hu, N. Murgovski, L. M. Johannesson, and B. Egardt, "Optimal Dimensioning and Power Management of a Fuel-Cell/Battery Hybrid Bus via Convex Programming," *IEEE/ASME Transactions on Mechatronics* 20, no. 1 (2015): 457–468.

10. X. Hu, C. Zou, X. Tang, T. Liu, and L. Hu, "Cost-Optimal Energy Management of Hybrid Electric Vehicles Using Fuel Cell/Battery Health-Aware Predictive Control," *IEEE Transactions on Power Electronics* 35, no. 1 (2020): 382–392.

11. G. Jinquan, H. Hongwen, L. Jianwei, and L. Qingwu, "Real-Time Energy Management of Fuel-Cell Hybrid Electric Buses: Fuel-Cell Engines Friendly Intersection Speed Planning," *Energy* 226 (2021): 120440.

12. A. M. Fernandez, M. Kandidayeni, L. Boulon, and J. P. Trovão, "Effects of Price Range Variation on Optimal Sizing and Energy Management Performance of a Hybrid Fuel Cell Vehicle," *IEEE Transactions on Energy Conversion* 38, no. 3 (2023): 1626–1638.

13. M. Kandidayeni, H. Chaoui, L. Boulon, S. Kelouwani, and J. P. F. Trovão, "Online System Identification of a Fuel Cell Stack With Guaranteed Stability for Energy Management Applications," *IEEE Transactions on Energy Conversion* 36, no. 4 (2021): 2714–2723.

14. A. T. Abkenar, A. Nazari, S. D. G. Jayasinghe, A. Kapoor, and M. Negnevitsky, "Fuel Cell Power Management Using Genetic Expression Programming in All-Electric Ships," *IEEE Transactions on Energy Conversion* 32, no. 2 (2017): 779–787.

15. A. Hajizadeh, M. A. Golkar, and A. Feliachi, "Voltage Control and Active Power Management of Hybrid Fuel-Cell/Energy-Storage Power Conversion System Under Unbalanced Voltage Sag Conditions," *IEEE Transactions on Energy Conversion* 25, no. 4 (2010): 1195–1208.

16. Y. Wang, S. J. Moura, S. G. Advani, and A. K. Prasad, "Power Management System for a Fuel-Cell/Battery Hybrid Vehicle Incorporating Fuel-Cell and Battery Degradation," *International Journal of Hydrogen Energy* 44, no. 16 (2019): 8479–8492.

17. G. A. M. Cuomo, "Report of the New York State Coordinating Council for Services Related and Other Dementias," (2019).

18. S. Sigfridsson, L. Li, H. Runvik, J. Gohl, A. Joly, and K. Soltesz, "Modeling of Fuel-cell Hybrid Vehicle in Modelica: Architecture and Drive Cycle Simulation," in *2nd Japanese Modelica Conference*, (Modelica Association, 2018): 91–98.

19. Z. Li, A. Yang, G. Chen, et al., "A Rapidly Reconfigurable DC Battery for Increasing Flexibility and Efficiency of Electric Vehicle Drive Trains," *IEEE Transactions on Transportation Electrification* 10, no. 2 (2023): 2322–2331.

20. S. Moussa and M. J. Ben Ghorbal, "Shepherd Battery Model Parametrization for Battery Emulation in EV Charging Application," in *2022 IEEE International Conference on Electrical Sciences and Technologies in Maghreb (CISTEM)*, (IEEE, 2022): 1–6.

21. O. Arteaga, H. Morales, H. Terán, et al., "Aerodynamic Optimization of the Body of a Bus," *IOP Conference Series: Materials Science and Engineering* 872, no. 1 (2020): 012002.

22. R. Rajamani, *Vehicle Dynamics and Control* (Springer, 2011).

23. J. R. Gardner, J. R. Gardner, and Z. L. Rendon, *XSLT and XPATH: A Guide to XML Transformations* (Prentice Hall Professional, 2002).

24. F. J. Vidal-Iglesias, J. Solla-Gullón, A. Rodes, E. Herrero, and A. Aldaz, "Understanding the Nernst Equation and Other Electrochemical Concepts: An Easy Experimental Approach for Students," *Journal of Chemical Education* 89, no. 7 (2012): 936–939.

25. M. N. Boukoberine, T. Donateo, and M. Benbouzid, "Optimized Energy Management Strategy for Hybrid Fuel Cell Powered Drones in Persistent Missions Using Real Flight Test Data," *IEEE Transactions on Energy Conversion* 37, no. 3 (2022): 2080–2091.

26. J. Snoussi, S. B. Elghali, M. Benbouzid, and M. F. Mimouni, "Optimal Sizing of Energy Storage Systems Using Frequency-Separation-Based Energy Management for Fuel-Cell Hybrid Electric Vehicles," *IEEE Transactions on Vehicular Technology* 67, no. 10 (2018): 9337–9346.

27. P. Bubna, D. Brunner, S. G. Advani, and A. K. Prasad, "Prediction-Based Optimal Power Management in a Fuel-Cell/Battery Plug-in Hybrid Vehicle," *Journal of Power Sources* 195, no. 19 (2010): 6699–6708.

28. M. Kandidayeni, A. O. M. Fernandez, A. Khalatbarisoltani, L. Boulon, S. Kelouwani, and H. Chaoui, "An Online Energy Management Strategy for a Fuel-Cell/Battery Vehicle Considering the Driving Pattern and Performance Drift Impacts," *IEEE Transactions on Vehicular Technology* 68, no. 12 (2019): 11427–11438.

29. P. Renna and S. Materi, "A Literature Review of Energy Efficiency and Sustainability in Manufacturing Systems," *Applied Sciences* 11, no. 16 (2021): 7366.

30. M. Ierides, R. de Valle, D. Fernandez, et al., "Advanced Materials for Clean and Sustainable Energy and Mobility," (2019).

31. A. Šmíd, "Comparison of Unity and Unreal Engine," (2017): 41–61, Czech Technical University in Prague (2017): 41–61.

32. H. Kumar, *Hydrogen Powered Cars and Trucks: Is There a Role for Them in the Electrified US Future?* (Massachusetts Institute of Technology, 2022).

33. J. R. Daduna and J. M. P. Paixão, "Vehicle Scheduling for Public Mass Transit—An Overview," in *Computer-Aided Transit Scheduling: Proceedings of the Sixth International Workshop on Computer-Aided Scheduling of Public Transport*, (Springer, 1995): 76–90.